Journal of Solid State Chemistry 181 (2008) 1642–1649

Contents lists available at ScienceDirect

Journal of Solid State Chemistry

journal homepage: www.elsevier.com/locate/jssc

Tomographic analysis of dilute impurities in semiconductor nanostructures

D.E. Perea [a], E. Wijaya [a], J.L. Lensch-Falk [a], E.R. Hemesath [a], L.J. Lauhon [a,b,*]

[a] Department of Materials Science and Engineering, Northwestern University, Evanston, IL 60208, USA
[b] Materials Research Center, Northwestern University, Evanston, IL 60208, USA

ARTICLE INFO

Article history:
Received 6 May 2008
Received in revised form
2 June 2008
Accepted 3 June 2008
Available online 7 June 2008

Keywords:
Atom probe
Nanowire
Semiconductor
Dopants
Impurities
Silicon
Germanium

ABSTRACT

We describe the application of pulsed-laser atom probe (PLAP) tomography to the analysis of dopants and unintentional impurities in Si and Ge nanowires grown by the vapor–liquid–solid mechanism. PLAP tomography was used to determine the concentration of phosphorous in Ge nanowires and B in Si nanowires, enabling comparisons of the atomic concentrations of the reactants with those of the reaction products. Oxygen impurities were also detected, but the contribution from background gas adsorption was not ruled out. Gold catalyst impurities were not detected, and an upper bound of 5 ppm was established. Intrinsic and extrinsic origins of the detection limits of dopants and other impurities are described in detail. A tapered nanowire geometry was found to improve the mass resolution and signal-to-noise ratio by increasing the tip cooling rate. Simulations of nanowire cooling under laser pulsing were used to validate this improved approach to PLAP analysis of nanowires.

1. Introduction

Semiconductor device technology will soon reach a point where continued scaling of device features becomes impractical due to the limitations in processing capabilities and costs [1]. To circumvent this, alternative technologies are being explored including the bottom-up synthesis and assembly of semiconductor nanowires. Interest in nanowires arises from the ability to precisely manipulate the synthesis conditions to produce unique 1D structures of controlled chemical composition, size, and morphology [2–4]. With these possibilities in mind, the exploration of the novel properties and potential applications of nanowires extends well beyond high performance-logic [5]. Although semiconductor whiskers were grown many decades ago [6], semiconductor nanowires are effectively a new material from the standpoint of electronic applications. Sophisticated electronic [7], photonic [8], and thermoelectric [9] devices with impressive performance have been demonstrated, but researchers are just beginning to develop fundamental insights into the relationships between the growth conditions, the composition and structure, and the resulting properties of nanowires. This paper describes recent developments in the analysis of nanowire composition and structure using pulsed-laser atom probe (PLAP) tomography. PLAP analysis of the dopant and impurity concentrations in Si and Ge nanowires indicate that atom probe tomography can play an important role in the development of semiconductor nanomaterials.

The current generation of complementary metal oxide semiconductor (CMOS) field-effect transistor technology relies on extremely precise control of dopant distribution, and equivalent or increased control is desired in the fabrication of nanowires to provide enhanced capabilities to tailor material properties and device characteristics. To fully understand the relationships between nanowire synthesis conditions and the resulting nanostructure, one would like metrological techniques capable of probing composition in three dimensions with nanoscale resolution. Transmission electron microscopy (TEM) and secondary ion mass spectrometry (SIMS) have traditionally provided the bulk of nanoscale structural and compositional information. SIMS, while sensitive to single ions, does not yet have nanoscale resolution in three dimensions [10,11] and conventional TEM is not generally capable of dopant mapping. The development of Z-contrast aberration-corrected scanning TEM has enabled the imaging of single impurity atoms [12,13], but the generality of the technique is limited by the fact that contrast of individual atoms scales as $Z^{1.7}$ [14], precluding imaging of, e.g., boron atoms in a silicon matrix.

Atom probe tomography provides a general approach to mapping the 3D composition of nanostructures, whether fabricated from bulk or directly synthesized. In addition, analysis of semiconductor materials is greatly facilitated by the implementation of

* Corresponding author at: Northwestern University, 2220 Campus Drive, Evanston, IL 60208, USA. Fax: +1 847 491 7820.
E-mail address: lauhon@northwestern.edu (L.J. Lauhon).

0022-4596/$ - see front matter © 2008 Elsevier Inc. All rights reserved.
doi:10.1016/j.jssc.2008.06.007

PLAP using the local electrode atom probe (LEAP) [15]. PLAP has been used, for example, to map the dopant distribution within the channel region of state-of-the art 20 nm transistors [15], the interfacial structure and chemistry in $In_xGa_{1-x}N$/GaN multiple quantum well structures [16], and the interfacial homogeneity of metal/oxide/metal magnetic tunnel junctions [17]. Most of the analyses performed to date have been concerned with thin-film materials with interesting nanostructures, but the technique is not restricted to thin-films. Recently, for example, the PLAP analysis of individual InAs [18] and Si [12] nanowires was demonstrated by the authors. To move beyond these proof-of-principle measurements, we have addressed at least three challenges that have hindered the routine analysis of dopant distributions in nanowire materials. The first challenge, which was partially addressed in Ref. [18], is the growth and preparation of nanowire specimens that meet the electrostatic requirements imposed by the LEAP. The second challenge is the limitation on the minimum detectable dopant concentration imposed by counting statistics, particularly because nanowires have small cross-sections. Ultimately, one would like to collect as many atoms as possible while minimizing background counts. The minimization of background counts is related to the third challenge—understanding the influence of the pulsed laser on the signal-to-noise ratio. Here we describe our recent progress in addressing these challenges so that other nanomaterials researchers will be able to take better advantage of new analytical capabilities offered by PLAP tomography. We note that we have applied the PLAP *technique* using the LEAP 3000X Si, which is a particular *instrument*.

2. Basic principles of LEAP analysis

First, we briefly describe the operating principles of a LEAP that are relevant to understanding the capabilities and specific limitations of nanowire analysis. The principles of operation inform the sample design, and are therefore important to review [18]. Generically, a positive bias of a few kV is applied between a cryogenically cooled needle-shaped specimen and a hollow conically shaped counter local electrode. The resulting electric field of tens of V/nm reduces the potential energy barrier for ion evaporation. A pulsed laser is focused on the specimen tip to induce thermally assisted field evaporation of a positively charged ion, after which the ion accelerates away from the specimen and toward a 2D position-sensitive detector. The mass-to-charge state ratio is calculated from the time delay between the application of the laser pulse and the detection of the ion, and the chemical identity of the ion is determined by analysis of peak positions within the resulting mass spectrum. The initial x- and y-position of the evaporated ion is established by reconstructing the flight path between the specimen tip and the detector. The z-position is determined from the sequence of single ion detection events. The evaporation, detection, and reconstruction processes are sufficiently well-defined that 3D composition maps can be obtained with sub-nanometer resolution. Greater understanding of and consensus on the influence of the laser on position and mass resolution has developed only recently [19] and we will return to this topic in a later section. In essence, one needs to adjust the static field and the pulsed laser energy such that no species evaporates in the absence of a laser pulse, and any species will evaporate in the presence of a laser pulse. In addition, the laser pulse energy should be sufficiently low to preclude surface diffusion of the specimen atoms.

The local electrode geometry enables analysis of specimens mounted on vertical arrays of posts pre-fabricated on planar substrates [20]. During analysis, the application of a bias between the local electrode and specimen creates the localized electric field. To minimize electrostatic shielding from the substrate and neighboring specimens, the specimen tip should be not less than ~50 μm from the substrate surface and neighboring specimens should be spatially separated by ~400 μm. Analyses of thin film semiconductor nanostructures are therefore typically performed on substrates consisting of microfabricated post arrays. Using a focused ion beam (FIB) and micromanipulation, selected areas of thin-film grown samples are removed and secured to a micropost top (commonly referred to as the lift-out technique) [21]. Annular milling is used to sharpen the specimen tip to the required radius.

3. Considerations for LEAP analysis of nanowires

The intrinsic needle-like shape of semiconductor nanowires suggests that nanowires can be ideal specimens for LEAP analysis provided the nanowires can be positioned vertically beneath the local electrode. Prior LEAP studies of semiconductor nanowires have demonstrated two possible growth strategies to meet the specimen geometry requirements specified above. In the first approach, Au catalyst disks were patterned by electron beam lithography, and arrays of vertical epitaxial InAs nanowires were grown directly on a high-conductivity planar GaAs(111)B substrates. These nanowires were analyzed using both voltage-pulsed [22] and laser-pulsed [18] LEAP tomography. The small diameters of nanowires pose a challenge to alignment as the nanowire must be centered beneath the local electrode with a precision of a few microns and the laser must be focused on the nanowire tip. Alignment can be facilitated by growing epitaxial nanowires on the pre-defined microposts mentioned above. Using this second approach, epitaxial Si nanowires of ~10 μm lengths were grown atop ~100 μm posts defined on Si(111) wafers [18]. The posts, with diameters of ~10 μm, are readily visible using a charge-coupled-detector (CCD) and telescope system, enabling the local electrode to be aligned to the micropost.

For the current study, Si and Ge nanowires were grown by the vapor–liquid–solid (VLS) process [6] on micropost array substrates fabricated from high conductivity Si(111) wafers using a deep reactive ion etching process [23]. A single micropost array substrate consists of a 10×10 array of 10 μm diameter posts 60–100 μm tall (Fig. 1). Following fabrication, the micropost array substrates were chemically etched in 30% KOH at 70 °C for 10 s, followed by a buffered HF etch and a standard RCA clean to remove contaminants from the wafer handling and processing [24]. To promote epitaxial growth along the [111] surface normal, we deposited gold nanoparticles from an acidified colloidal

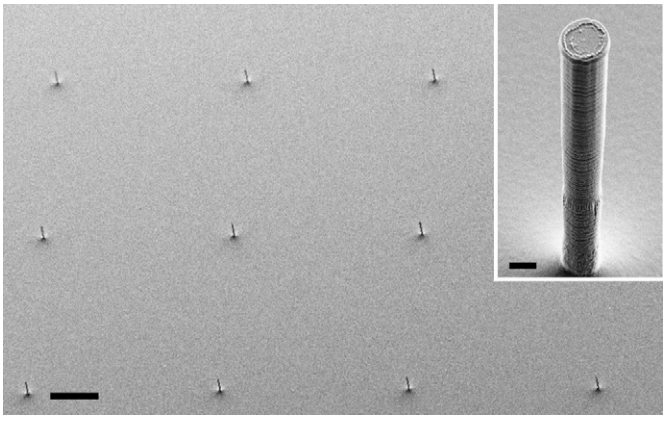

Fig. 1. Scanning electron microscope (SEM) image of a micropost array used for the epitaxial growth of semiconductor nanowires for LEAP analysis; the scale bar is 100 μm. The image is taken at a 35° tilt normal to the substrate. The inset shows an individual micropost; the scale bar is 3 μm.

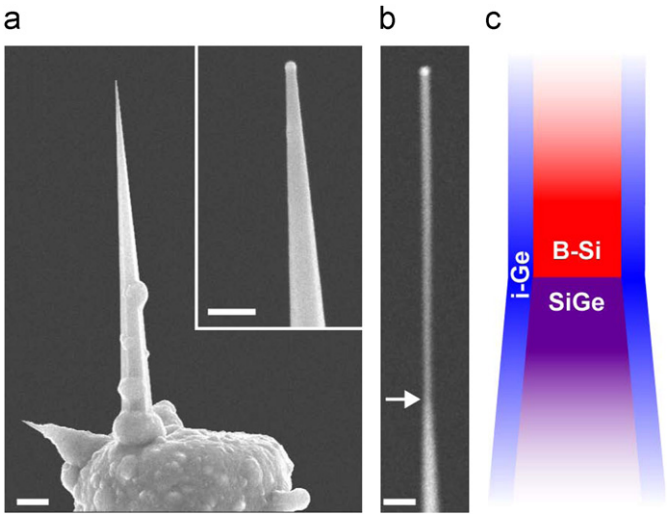

Fig. 2. Epitaxial (a) P-doped Ge nanowire (scale bar 1 μm) and (b) a B-doped Si nanowire (scale bar 100 nm) grown atop a microposts. The Au catalyst nanoparticle can be seen at the tip of the wires as shown in the inset of (a) (scale bar 200 nm) and in (b). (c) Schematic of local region centered at arrow in (b) illustrating nanowire structure. The details of the structure are discussed in the text.

solution as described by Woodruff et al. [25]. Using this deposition technique and the growth conditions specified below, it is possible to achieve ~90% yield of vertically oriented Ge nanowires from 30 nm catalyst particles.

Si and Ge nanowires were grown in a thermal chemical vapor deposition reactor using silane (SiH_4) and germane (GeH_4) as source gases and phosphine (PH_3) and diborane (B_2H_6) as dopant gases. The Ge and Si nanowires discussed in this study were grown at 380 and 450 °C, respectively. For Ge nanowires, GeH_4 and He flow rates were 2 and 38 sccm, respectively, and the total reactor pressure was 50 Torr. For Si nanowires, SiH_4 and N_2 flow rates were 2 and 50 sccm, respectively, and the total reactor pressure was 50 Torr. Ge nanowires grown under these conditions are tapered due to decomposition of germane on the sides of the nanowires, whereas Si nanowires are untapered because silane is more stable than germane. Fig. 2a shows a scanning electron microscope (SEM) image of a tapered Ge nanowire. The tapered shape provides additional mechanical stability to the nanowire under analysis, which reduces the rate of fracture from the high strains imposed by the biasing conditions. The taper provides an additional benefit for PLAP analysis that will be discussed further below. For these reasons, the Si nanowires analyzed here were grown atop tapered SiGe bases, as shown in Fig. 2b and c. The schematic in Fig. 2c also shows the presence of a Ge shell, which will be discussed in the next section. Prior to PLAP analysis, the specimens were cryogenically cooled to 60–80 K. Laser pulses of 10 ps width from a 532-nm laser were focused on the nanowire tip. A pulse frequency of 100 kHz, pulse energy of 0.02–0.1 nJ, and evaporation rate of 0.5% were used consistently throughout the analysis.

4. Analysis of dopant concentration

Here we describe the first quantitative determination of the dopant concentration in a semiconductor nanowire using PLAP tomography. Measurement of the concentration and distribution of dopant atoms is of fundamental importance to the advancement of the understanding and control of materials properties. PLAP analysis was performed on Ge nanowires that were doped with phosphorous by introducing phosphine into the reactor

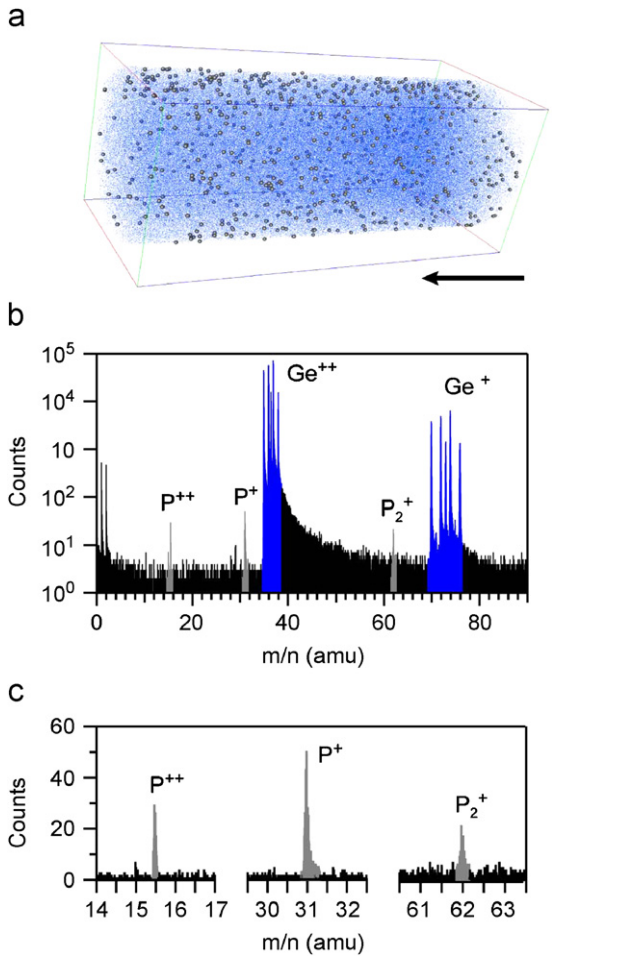

Fig. 3. P dopants within a Ge nanowire. (a) 3D reconstruction of a selected volume of a P-doped Ge nanowire. The blue dots are germanium and the gray spheres are phosphorus. Reconstruction dimensions are $45 \times 45 \times 75\ nm^3$. For clarity only 25% of the total Ge atoms are shown; 100% of the P atoms are shown. Arrow indicates nanowire growth direction. (b) Mass spectrum associated with reconstruction shown in (a). (c) Selected regions of mass spectrum showing P related peaks.

during VLS growth. Fig. 3a shows a selected volume reconstruction of an experimental run in which ~6 million ions were collected from a single nanowire. The associated mass spectrum (Fig. 3b) is presented as a histogram of the number of detected events of a given mass-to-charge state ratio (m/n) in bins 0.01 amu in width. Each ion that is associated with a known species in the spectrum, i.e., corresponds to an identified peak, is represented by a single color-coded dot in the reconstruction. Ge^+ and Ge^{2+} peaks are the most visible features of the spectrum, and the five naturally occurring isotopes are clearly resolved for each of the two charge states. There are several other peaks in the mass spectrum associated with the P dopant atoms, including P^{2+} (15.5 amu), P^+ (31 amu), and P_2^+ (62 amu); the respective peaks are highlighted in Fig. 3c. The detection of small clusters such as P_2^+ is not uncommon in PLAP [26]. Phosphorus has only one naturally occurring isotope and so occurs as a single peak.

To determine the P concentration, the counts within m/n ranges associated with P are summed and divided by the corresponding sum of counts associated with Ge, leading to a concentration of $1.0 \pm 0.2 \times 10^{18}\ cm^{-3}$ for the sample shown in Fig. 3. The background count rate adjacent to each peak is subtracted prior to the summation of counts within a given mass window. Due to the large number of Ge counts, the uncertainty in the concentration is dominated by the uncertainty in the P counts, and the background counts in turn strongly influence the

uncertainty in the dopant concentration. The largest source of background counts is the "thermal tail" associated with the Ge peaks. The nature of this tail and other sources of background counts will be discussed in detail below, but we note that the ability to detect an impurity may be influenced by the relative positions of the impurity and host peaks. We also note that the concentration of P in the nanowire does not correspond to the relative ratio of P to Ge in the gas phase because the respective precursor decomposition and atom incorporation rates are not identical. The P concentration in the central "core" portion of the nanowire shown here, for example, is ~30 ppm, whereas the gas phase concentration is 1000 ppm. A detailed study of the phosphorous concentration and distribution will be reported in another publication; the present result establishes the capability.

We next consider the concentration of boron atoms in Si nanowires doped using B_2H_6 to provide a comparison measurement of a dopant concentration in a different material. Doped Si nanowires of ~1 μm length were grown atop tapered SiGe nanowire bases using silane and diborane at a gas phase Si:B ratio of 667 ppm. Immediately following Si nanowire growth, an intrinsic Ge shell was grown, as shown schematically in Fig. 2c. The shell serves two purposes. First, it acts as a radial marker layer for the extent of the Si nanowire core. Second, it can enable the entire nanowire diameter to be captured within the LEAP detector; by increasing the nanowire radius, the magnification is decreased, i.e., a larger fraction of the Si core is projected onto the finite solid angle of the detector. A portion of the LEAP tomographic reconstruction of a doped Si nanowire is shown in Fig. 4a. Si and Ge atoms are indicated by red and blue dots, respectively, and boron atoms are indicated by green spheres. The selected volume contains portions of both the B-doped Si core (red) and the Ge shell (blue). The mass spectrum of the entire sample (Fig. 4b) is dominated by peaks associated with Si and Ge. Silicon has three naturally occurring isotopes that are evident in both the Si^{2+} (14, 14.5, 15 amu) and Si^{+} (28, 29, 30 amu) peaks.

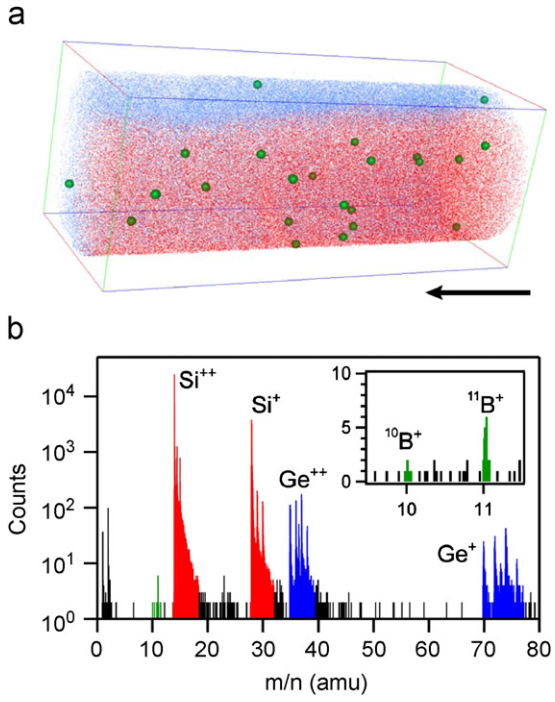

Fig. 4. B dopants within a Si nanowire. (a) 3D reconstruction of a portion of a B-doped Si nanowire (red = silicon; blue = germanium, green = boron). Reconstruction dimensions: $23 \times 23 \times 45\,nm^3$. For clarity, only 25% of the total Si and Ge atoms are shown. Arrow indicates nanowire growth direction. (b) Mass spectrum associated with the reconstruction shown in (a). Inset: B isotope peaks.

Boron has two naturally occurring isotopes at 10 and 11 amu, each of which is evident in the inset of Fig. 4b. To determine the concentration of B in Si, a sub-volume encompassing only the Si core was isolated and the associated mass spectrum (not shown) was analyzed. The B concentration was determined to be $1.1 \pm 0.2 \times 10^{19}\,cm^{-3}$ (~200 ppm), which is slightly less than the ratio of B to Si in the gas phase precursors. The increased relative concentration of B in Si compared to P in Ge is consistent with the relative stability of the precursors in question, but additional factors may influence incorporation rates across the liquid–solid interface. It is important to note that LEAP analysis cannot determine the fraction of electrically active dopant atoms because the substitutional or interstitial nature of the impurity atom cannot be discerned. Clusters of dopant atoms can in principle be distinguished from isolated dopant atoms, however.

5. Analysis of unintentional impurity concentration

Unintentional impurities can strongly influence the electronic properties of semiconductors, and are therefore also important targets of composition analysis. As with thin films, background gases in the reactor containing oxygen or carbon might become incorporated into nanowires during growth. In addition, nanowires grown by an impurity-mediated process, such as VLS, may contain impurity atoms incorporated from the catalyst particles themselves. Gold, for example, creates deep-level traps which act as recombination centers in Si and Ge adversely affecting nanowire transport [27]. We previously established upper bounds on the gold concentration in silicon nanowires grown by a VLS process [18]. More recently, individual gold atoms were imaged within VLS-grown silicon nanowires using aberration-corrected high-angle annular dark field imaging in a scanning transmission electron microscope [12,28]. Here we establish an upper bound on the gold concentration in Ge nanowires, and discuss challenges to measurement of the oxygen concentration.

Fig. 5a shows the reconstruction of a gold-catalyzed phosphorous-doped Ge nanowire. The gold catalyst is seen at the left side of the figure. Mass spectra were extracted from cylindrical subvolumes localized within the catalyst (red cylinder, Fig. 5a) and nanowire (blue cylinder, Fig. 5a); the mass spectra in the vicinity of Au^{+} (197 amu) and Au^{2+} (98.5 amu) are plotted for the catalyst and nanowire regions in Fig. 5b and c respectively. The mass spectrum of the Ge nanowire does not exhibit a peak in the Au^{+} or Au^{2+} regions, which are highlighted. The subtraction of a constant background count rate in the vicinity of these peaks produces an average of zero counts per bin. The absence of a distinct peak does not preclude the presence of a low-level impurity, but it does enable the determination of an upper bound on the concentration of the impurity. In the absence of a peak, we consider the root mean squared (RMS) fluctuation of the background as the uncertainty in excess Au counts. Dividing this uncertainty by the total number of Ge counts gives an upper bound on the gold concentration. The upper bound of Au within the bulk of the Ge nanowire (Fig. 5c) was thereby calculated to be $2 \times 10^{17}\,cm^{-3}$. As with the dopant atoms, this uncertainty is ultimately determined by the average background count rate in the spectral regions of interest. The origins of the background counts and approaches to minimizing the background count rate are the subject of the next section.

Impurities such as oxygen and carbon could also be present in nanowires because gases containing these atoms are present at some finite level during growth. Fig. 6 shows an end-view of a Ge nanowire along with mass spectra selected from the outer and inner portions of the nanowire. The reconstruction (Fig. 6a) reveals the presence of a native oxide layer on the outside of the

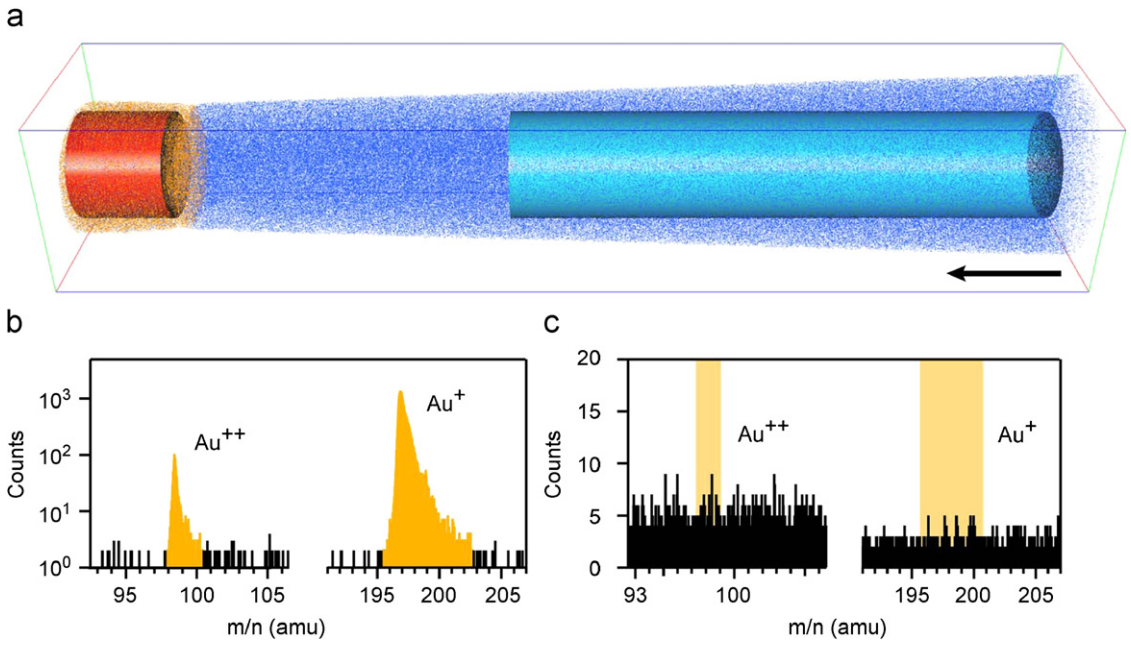

Fig. 5. Au catalyst impurities within a Ge nanowire. (a) Reconstruction of a Ge nanowire. Yellow dots = Au; blue dots = Ge. Reconstruction dimensions: $42 \times 42 \times 235\,nm^3$. For clarity, only 10% of the Ge and Au atoms are shown. Arrow indicates nanowire growth direction. (b) Mass spectrum from within the gold catalyst (region defined by the red cylinder). (c) Mass spectrum within the nanowire (region defined by the blue cylinder). The sections where Au peaks would appear are highlighted.

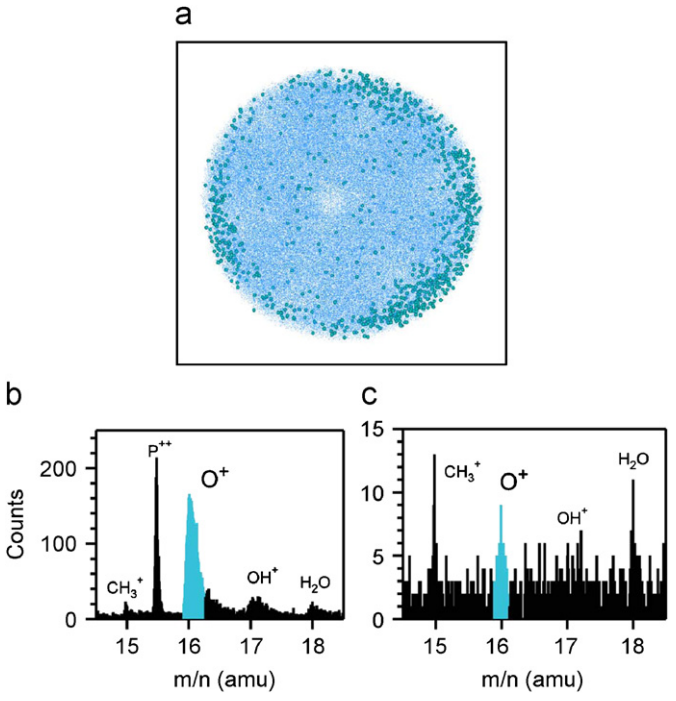

Fig. 6. Oxygen atoms in a Ge nanowire. (a) End view of a P-doped Ge nanowire. Light blue dots = Ge; blue spheres = O. Bounding box dimensions: $42 \times 42\,nm^2$. (b) Mass spectrum from the outer region of (a). (c) Mass spectrum from the inner portion of the reconstruction in (a).

nanowire within the field of view. The mass spectrum from this outer region of the nanowire (Fig. 6b) contains an O^+ peak (16 amu) due to the oxide, as well as smaller adjacent peaks that are assigned to CH_3^+ or NH^+ (15 amu), OH^+ (17 amu), and H_2O^+ (18 amu). These latter peaks are assumed to arise from adsorption and evaporation of background gases [29]. The mass spectrum from the inner portion of the nanowire (Fig. 6c) also exhibits a peak at 16 amu, which we attribute to atomic oxygen. It would be premature to claim that the observed oxygen counts arise only from oxygen dissolved in the nanowire during growth because the relative magnitude of the adjacent peak at 15 amu suggests that contribution from background gases during analysis cannot be ruled out. Background gases therefore present a potential extrinsic source of error in the determination of dilute impurity concentrations, as discussed in more detail below. In future work, we intend to analyze a Ge sample fabricated from a bulk wafer of known oxygen concentration sequentially with a nanowire sample to address the issue of oxygen incorporation during VLS nanowire growth.

6. Origin of impurity detection limits

The detection limit of a given impurity in PLAP analysis has both intrinsic and extrinsic origins. Counting statistics impose an ultimate intrinsic limit that depends on the number of atoms or volume analyzed. In a background-free spectrum containing 1 million total atoms, for example, the detection of 100 impurity atoms corresponds to an impurity concentration of 100 ± 10 part per million, with the uncertainty given by the square root of the number of impurity atoms detected. Typical nanowire runs produce datasets of 1–10 million counts spanning 10's to 100's of nanometers of nanowire length, so the detection limit thus far has been intrinsically limited to values greater than 1 ppm simply due to counting statistics.

The detection limit is also extrinsically limited by sources of background noise as with other spectroscopic techniques. The error associated with the counting of a large number of events within an arbitrary range is calculated as the square root of the total counts, i.e. all counts within a peak. It follows that as the number of background counts increases, the relative error associated with the excess background-subtracted counts increases. Here we consider several specific sources of such noise in the PLAP measurement. Ultra-high vacuum systems contain residual gases, including H_2, CO, and CO_2. Background gas atoms which adsorb on the specimen tip may be field evaporated during the laser pulse. Such events can be identified in the mass

spectrum and can be excluded from the composition analysis unless they happen to coincide with specimen peak of interest. For example, hydrogen peaks are seen at 1 amu (H^+) and 2 amu (H_2^+) in the mass spectra of Fig. 3b and 4b. Residual gas atoms can also undergo field evaporation as a result of the standing voltage *in between* laser pulses. Such events are uncorrelated and appear as background noise distributed throughout the spectrum [30], thereby raising the detection limit. The arrivals of the ions are randomly distributed in time, which produces a background noise distribution proportional to the inverse square root of the mass of the evaporated atom [31]. As such, the detection of small mass impurities is affected more than that of larger mass impurities. These events can never be eliminated, but can be minimized by minimizing the chamber pressure and optimizing the relative magnitudes of the standing voltage and laser pulse energy.

Two other processes contribute to similarly distributed counts. First, atoms and molecules adsorbed on the shank of the nanowire may diffuse to the apex region where ionization occurs [30]. Second, atoms from the nanowire itself may evaporate in between laser pulses if the standing voltage is too high for a given tip temperature. In fact, the "tails" in the major peaks of the mass spectra shown here arise from the evaporation of Si and Ge atoms long after the laser pulse, with the count rate decaying on a time-scale determined by the cooling rate of the nanowire tip. This suggests that control over tip cooling is essential to maximizing the sensitivity of a PLAP measurement. Although there is some debate regarding the mechanism of femtosecond pulsed laser-assisted field-evaporation, it has been shown that picosecond pulsed laser field-evaporation proceeds via a thermal rather than athermal mechanism [19]. In the next section, we consider the influence of the specimen geometry on tip cooling and by extension, the extrinsically determined detection limits of LEAP tomography.

7. Role of laser heating and influence of specimen geometry

To understand the role of laser heating in PLAP analysis and how its effects might be controlled, we first describe the evaporation process in more detail. The mass spectrum is a representation of the number of detected ions within given ranges of flight times. The flight times are converted to mass-to-charge ratios and binned in increments of 0.01 amu for the spectra shown here. Pulsed laser-assisted field-evaporation and subsequent detection of ions produces peaks with very sharp leading edges and more slowly decaying tailing edges. The sharp leading edge results from the rapid rise in temperature and subsequent onset of ion evaporation associated with the absorption of energy from the laser pulse; the thermal pulse excites the atoms over the energy barrier to desorption, commonly referred to as the Schottky hump, the height of which depends on the applied electric field at the specimen tip. The tail in a given mass peak decays more slowly, as the decay is associated with the cooling of the specimen tip. The peak width, or mass resolution, will therefore depend on the rate at which the specimen tip cools down to the base temperature. For materials with low thermal conductivity, the specimen tip cools down more slowly, and continued evaporation after the laser pulse leads to long "thermal" tails in the peaks of mass spectra. If these thermal tails overlap other mass peaks of interest, the uncertainty in the concentration of these other species will be increased.

The thermal conductivity of Si and Ge nanowires is greatly diminished compared to the bulk values due to substantial surface scattering of phonons [32]. As a consequence, we have observed that the PLAP mass spectra of long untapered Si nanowires exhibit very long thermal tails, as shown for the Si^{2+} and Ge^{2+} peaks in

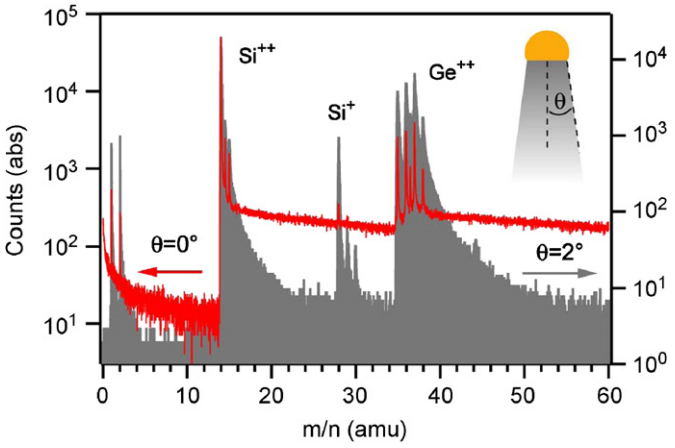

Fig. 7. Comparison of mass spectra from tapered and untapered nanowires. The taper angle is defined in the inset schematic. The red (unfilled) mass spectrum is from an untapered ($\theta = 0^\circ$) nanowire and exhibits excessive thermal tailing from both Si^{2+} and Ge^{2+}. The gray (filled) mass spectrum is from a nanowire with a 2° taper angle and exhibits rapidly decaying thermal tails.

Fig. 7 (red spectra). Such tails can inhibit detection of important impurities such as P (31 amu). This situation can be improved by intentionally growing tapered nanowires to increase the shank angle of the specimen [19]. Fig. 7 also shows a Si nanowire spectrum (gray) with a non-zero shank angle for which the thermal tail is shorter and background noise level is reduced. The tip cooling is clearly much faster for the tapered nanowire for two reasons. First, the larger cross-sectional area towards the base increases the conduction of heat away from the tip. Second, the reduction in thermal conductivity due to surface phonon scattering diminishes as the nanowire diameter increases [32] away from the tip. As discussed further below, the laser spot size also influences the tip cooling rate. The ideal laser spot size would be the smallest spot that produces uniform heating across the very end of the specimen.

The time scale of tip cooling can be related to the half-width at half-maximum (HWHM) in a mass spectrum as follows. The mass-to-charge ratio in time-of-flight mass spectrometry is given by

$$\frac{m}{n} = k(\alpha V_{\mathrm{dc}} + \beta V_{\mathrm{pulse}})\left(\frac{t - t_0}{d}\right)^2,$$

where k is a constant ($= 1.92972 \times 10^{-4}$ amu mm^2 V^{-1} ns^{-2}) and α, β, d, and t_0 are instrument-specific parameters [30]. This expression relates to the voltage-pulsed mode of operation, but the time dependence is the same for laser-pulsed operation. For small intervals in time and mass,

$$\Delta t \approx \frac{d}{2\sqrt{k\alpha V_{\mathrm{dc}}}} \frac{\Delta(m/n)}{\sqrt{(m/n)}} \propto \frac{1}{\sqrt{m}} \Delta m.$$

This expression shows that the larger the mass-to-charge ratio of a given species, the wider its peak in the mass spectra (e.g. compare Au^+/Au^{2+} peaks in Fig. 5b). If one considers the widths of the Ge^{2+} and Ge^+ peaks in the spectra of Fig. 3b as empirically acceptable, then one may prescribe that the tip should cool to a temperature halfway between the base and peak temperatures in ~10 ns. If the tip cooling is significantly slower, long thermal tails in the mass spectra may degrade the resolution of peaks on the high mass side of an adjacent peak, such as P (31 amu) next to Si (28, 29, and 30 amu).

To evaluate the effect of shank angle on the mass spectra more quantitatively, and develop prescriptions for optimized PLAP analysis, we simulated the tip cooling of 30 nm diameter, 10-μm-long Si nanowires with increasing shank angles of 0°, 1°,

2°, and 4°, using commercial finite element modeling software [33]. We assume that the initial temperature profile of the specimen follows the Gaussian profile of the laser beam intensity with a laser spot of 1.0 μm full-width at half the maximum intensity. This assumption is justified by the fact that there is negligible heat transport during the ~10 ps that the sample is illuminated by the laser pulse [34]. The base temperature is held constant at 70 K, and we assume that absorption of the laser pulse results in a peak temperature of 250 K at the nanowire tip; several authors have suggested that the peak temperatures under similar experimental conditions with comparable evaporation rates lie in the range of 200–400 K [35–37]. Thermal conductivity of Si and Si/SiGe superlattice nanowires has been observed to depend on size and temperature [32,38]. In our simulation of tapered nanowires, we assumed a spatially varying thermal conductivity interpolated from the experimentally published values [38]. We neglected the temperature dependence because the thermal conductivity shows little variation in the temperature range of interest (70–250 K) for nanowire diameters comparable to those studied here.

The results of the simulation are shown in Fig. 8. For the purposes of discussion, we will examine the time required for the tip temperature to return to 160 K, which is halfway between the base temperature and the peak temperature. The difference in cooling rates between nanowires with tapers of 0° and 4° is dramatic. With a 4° taper, the tip cools to 160 K within 6 ns. With a 0° taper, the tip reaches 160 K only after ~50 ns. Results for a range of angles are summarized in Table 1. Empirically, we have found that a taper of 2° or larger is needed for Si and Ge nanowires to evaporate with acceptable thermal tails. In the simulation, the specimen with a 2° taper cools to 160 K within 8.5 ns, in reasonable agreement with our empirical findings. Taper also affects tip cooling at long time scales. For tapers of 2° and larger, the tip cools to the base temperature within ~100 ns. In contrast, the untapered nanowire returns to the base temperature only after ~4 μs (Fig. 8, inset), limiting the pulsing frequency to $\sim(4\,\mu s)^{-1} = 250$ kHz; at higher pulse frequencies the base temperature would steadily rise, leading to steady-state evaporation of ions and background noise distributed across the mass spectrum. In addition, the elevated base temperature decreases the cooling rate, which degrades the mass resolution. Cerezo et al. [31] have described this degradation of mass resolution with increased pulsing frequency. The pulsing frequency used for the measurements described here was 100 kHz, which is sufficient to allow the nanowire to cool completely between laser pulses.

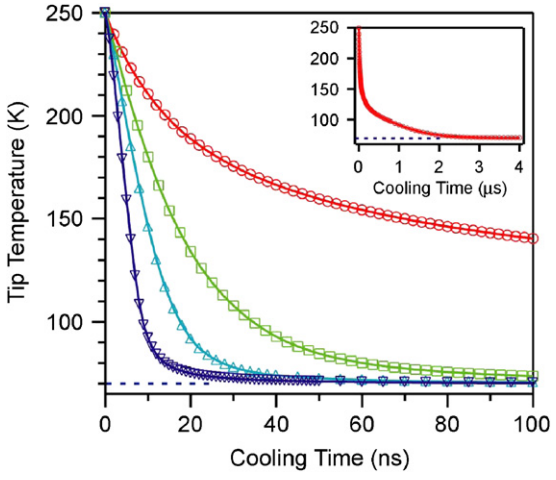

Fig. 8. Comparison of nanowire tip cooling time as a function of taper angle. Red circles, 0°; green squares, 1°; light blue triangles, 2°; dark blue inverted triangles, 4°. The inset shows the temperature over 4 μs for the 0° wire. Dashed line highlights 70 K base temperature.

Table 1
Time (ns) for nanowire tip to cool to 160 K and 70 K versus taper angle

Temp.	0°	1°	2°	4°
160 K	49	14	8.5	5
70 K	4000	400	100	50

In general, nanowires synthesized for device applications do not have a tapered cross-section, and one would like to directly compare PLAP analyses with the electrical properties of nanowires grown under the same conditions. To achieve this objective, while simultaneously optimizing the PLAP analysis, we have adopted a hybrid specimen geometry consisting of an untapered nanowire on a tapered base, as shown in Fig. 2b and c. The effectiveness of this approach is validated by cooling simulations of a hybrid 500-nm-long untapered SiNW with a 30-nm tip diameter grown on a 9.5-μm-long tapered base with 4° taper angle. Comparisons of the hybrid nanowire temperature with that of uniformly tapered nanowires (Fig. 9) indicate that the tapered base is effective in cooling the untapered analysis region, provided that the length of untapered analysis region is less than ~1 μm. The effects can be seen more clearly in the cooling rates dT/dt shown in the inset of Fig. 9. The initial cooling rate for the hybrid geometry is comparable to the 0° taper angle case because most of the thermal energy is concentrated in the untapered section. As soon as the heat from the tip diffuses to the tapered region of higher thermal conductivity, the cooling rate increases dramatically. While the 1° taper angle tip initially cools more quickly than the hybrid tip, the hybrid tip is almost fully cooled by 30 ns.

The effect of the laser spot size, also examined in Fig. 9, is straightforward to interpret. For evaporation of single ions, only the very tip of the nanowire needs to reach the threshold for thermally assisted field evaporation. The smaller the width of the laser spot, the smaller the volume of nanowire that is heated, and the more rapidly that heat from the tip can be dissipated. The quantitative effects of spot size on short- and long-time cooling rates are summarized in Table 2. Recalling that the width of the thermal tail of a given peak is related to the tip cooling at short time-scales, we see that a reduction of the laser spot size from 1.0

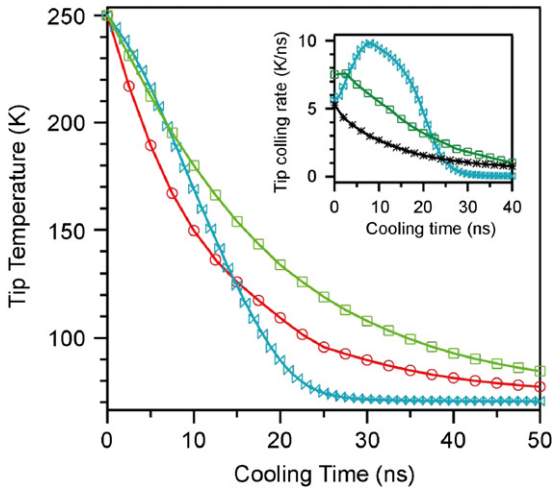

Fig. 9. Comparison of tip cooling time as a function of taper angle and laser spot size. Green squares, 1°shank/1.0 μm spot; red circles, 1°shank/0.5 μm spot; light blue double triangle, hybrid taper/1.0 μm spot. The inset shows the nanowire tip cooling rate (dT/dt) for hybrid/1.0 μm (light blue double triangle), 1°shank/1.0 μm spot (green squares), and 0°shank/1.0 μm spot (black asterisks).

Table 2
Time (ns) for nanowire tip to cool to 160 K versus taper angle for different laser spot sizes

Laser spot size	0°	1°	Hybrid	4°
1.0 μm	49	14	11	5
0.5 μm	24	8.5	8.8	3.3

to 0.5 μm, while maintaining the same evaporation rate, reduces the temporal width of the thermal tail by 20% in the case of hybrid specimen geometry and 50% for the untapered nanowire. This is in qualitative agreement with the findings of Bunton et al. [19], where an improvement in the mass resolving power was found using a laser spot size of 2.5 μm as compared to 5.0 μm. In addition, there is a benefit to reducing the laser spot size that is not captured by the simulation. Surface adsorbates can be induced to diffuse and evaporate even under weak excitation in the tails of the laser spot. A reduction in spot size reduces this contribution to background noise as well [39].

In summary, experiments and related simulations of PLAP analysis of nanowires indicate that a tapered geometry improves mass resolution and reduces background counts, as large enhancements in tip cooling are realized at taper angles of only a few degrees. The hybrid geometry described here is one approach to achieving acceptable mass spectra from device-relevant nanowires. Finally, improvements in beam focusing optics and reductions in wavelength could lead to reductions in the laser spot size, which would also improve the cooling rate and lower the detection limit of intentional and unintentional impurities.

8. Prospects for impurity mapping in nanowires

We have shown that PLAP tomography using the LEAP is an effective approach to determining dopant concentrations in Si and Ge semiconductor nanowires. Because the technique is tomographic, the dopant distributions can also be determined and will be described in subsequent publications. To date, no other methods have been able to determine both the concentration and distribution of dilute impurities within a nanostructured semiconductor. Prospects for analysis of unintentional impurities are also very good, though impurities with peaks that overlap peaks from residual background gases will require more detailed analysis and control measurements to extract reliable concentrations. We expect PLAP tomography to play an important role in the development of the fundamental understanding and applications of semiconductor nanowires.

Acknowledgement

The work was supported by the National Science Foundation through the CAREER and NIRT programs and by the Office of Naval Research. D.E.P. acknowledges the support of a Ford Foundation Fellowship, J.L.L. acknowledges the support of an NSF graduate fellowship, and L.J.L. acknowledges the support of an Alfred P. Sloan Research Fellowship. The assistance of B. Rob Ilic and Meredith Metzler in the microfabrication of the micropost array substrates at the Cornell NanoScale Science and Technology Facility (CNF) is acknowledged. Atom probe measurements were performed at the Northwestern Center for Atom Probe Tomography (NUCAPT). The LEAP microscope was purchased with funding from the NSF-MRI (DMR-0420532) and ONR-DURIP (N00014–0400798) programs. We acknowledge the Northwestern University Atomic and Nanoscale Characterization Center for the use of the microscopy facilities, and Tom Kelly and David Larson of Imago Scientific Instruments for useful discussions.

References

[1] A. Wolfgang, P. Cogez, M. Graef, H. Ishiuchi, T. Osada, J. Moon, R. JaeSung, H.-C. Sohn, W. Yang, M.-S. Liang, C. H. Diaz, C.-H. Lin, P. Apte, B. Doering, P. Gargini, International Technology Roadmap for Semiconductors; Executive Summary, 2007.
[2] L.J. Lauhon, M.S. Gudiksen, C.L. Wang, C.M. Lieber, Nature 420 (2002) 57–61.
[3] M. Law, J. Goldberger, P.D. Yang, Annu. Rev. Mater. Res. 34 (2004) 83–122.
[4] M.S. Gudiksen, L.J. Lauhon, J. Wang, D.C. Smith, C.M. Lieber, Nature 415 (2002) 617–620.
[5] W. Lu, C.M. Lieber, Nat. Mater. 6 (2007) 841–850.
[6] R.S. Wagner, W.C. Ellis, Appl. Phys. Lett. 4 (1964) 89–90.
[7] C. Thelander, P. Agarwal, S. Brongersma, J. Eymery, L.F. Feiner, A. Forchel, M. Scheffler, W. Riess, B.J. Ohlsson, U. Gosele, L. Samuelson, Mater. Today 9 (2006) 28–35.
[8] P.J. Pauzauskie, P. Yang, Mater. Today 9 (2006) 36–45.
[9] A.I. Boukai, Y. Bunimovich, J. Tahir-Kheli, J.K. Yu, W.A. Goddard, J.R. Heath, Nature 451 (2008) 168–171.
[10] M.C. Putnam, B.M. Kayes, M.A. Filler, M.D. Kelzenberg, Y. Guan, N.S. Lewis, J.M. Eiler, H.A. Atwater, MRS Spring Meeting, San Francisco, CA, 2008.
[11] C.J. Simensen, O. Nielsen, F. Hillion, J. Voje, Metall. Trans. A 38A (2007) 1448–1451.
[12] J.E. Allen, E.R. Hemesath, D.E. Perea, J.L. Lensch-Falk, Z.Y. Li, F. Yin, M.H. Gass, P. Wang, A.L. Bleloch, R.E. Palmer, L.J. Lauhon, Nat. Nanotechnol. 3 (2008) 168–173.
[13] A.J. D'Alfonso, S.D. Findlay, M.P. Oxley, S.J. Pennycook, K. Van Benthem, L.J. Allen, Ultramicroscopy 108 (2007) 17–28.
[14] P.M. Voyles, D.A. Muller, J.L. Grazul, P.H. Citrin, H.J.L. Gossmann, Nature 416 (2002) 826–829.
[15] T.F. Kelly, D.J. Larson, K. Thompson, R.L. Alvis, J.H. Bunton, J.D. Olson, B.P. Gorman, Annu. Rev. Mater. Res. 37 (2007) 681–727.
[16] M.J. Galtrey, R.A. Oliver, M.J. Kappers, C.J. Humphreys, D.J. Stokes, P.H. Clifton, A. Cerezo, Appl. Phys. Lett. 90 (2007) 061903.
[17] D.J. Larson, Thin Solid Films 505 (2006) 16–21.
[18] D.E. Perea, J.L. Lensch, S.J. May, B.W. Wessels, L.J. Lauhon, Appl. Phys. A Mater. Sci. Process. 85 (2006) 271–275.
[19] J.H. Bunton, J.D. Olson, D.R. Lenz, T.E. Kelly, Microsc. Microanal. 13 (2007) 418–427.
[20] T.F. Kelly, D.J. Larson, Mater. Charact. 44 (2000) 59–85.
[21] K. Thompson, D. Lawrence, D.J. Larson, J.D. Olson, T.F. Kelly, B. Gorman, Ultramicroscopy 107 (2007) 131–139.
[22] D.E. Perea, J.E. Allen, S.J. May, B.W. Wessels, D.N. Seidman, L.J. Lauhon, Nano Lett. 6 (2006) 181–185.
[23] The microfabrication processing of the micropost array substrates was performed at the Cornell NanoScale Science & Technology Facility (CNF).
[24] The RCA cleaning consisted of a series of 3 chemical etches. (1) organic clean: H_2O:NH_4OH:H_2O (5:1:1) @ 75 °C, 10 min, (2) oxide strip: H_2O:HF (50:1) @ 25 °C, 15 s, (3) ionic clean: H_2O:HCl:H_2O_2 (6:1:1) @ 75 °C, 10 min. A 1 min. DI water rinse was done after each etch.
[25] J.H. Woodruff, J.B. Ratchford, I.A. Goldthorpe, P.C. McIntyre, C.E.D. Chidsey, Nano Lett. 7 (2007) 1637–1642.
[26] M.K. Miller, G.D.W. Smith, Atom Probe Microanalysis: Principles and Applications to Materials Problems, Materials Research Society, Pittsburgh, 1989.
[27] W.M. Bullis, Solid-State Electronics 9 (1966) 143–168.
[28] S.H. Oh, K.v. Benthem, S.I. Molina, A.Y. Borisevich, W. Luo, P. Werner, N.D. Zakharov, D. Kumar, S.T. Pantelides, S.J. Pennycook, Nano Lett. 8 (2008) 1016–1019.
[29] A potentially significant source of water may come from water dissolved in the surface oxide which is known to be water soluble.
[30] M.K. Miller, Atom Probe Tomography: Analysis at the Atomic Level, Kluwer Academic/Plenum Publishers, New York, 2000.
[31] A. Cerezo, P.H. Clifton, A. Gomberg, G.D.W. Smith, Ultramicroscopy 107 (2007) 720–725.
[32] D.Y. Li, Y.Y. Wu, P. Kim, L. Shi, P.D. Yang, A. Majumdar, Appl. Phys. Lett. 83 (2003) 2934–2936.
[33] Comsol Multiphysics v3.4
[34] M.K. Miller, A. Cerezo, M.G. Hetherington, G.D.W. Smith, Atom Probe Field Ion Microscopy, Claredon Press, Oxford, 1996.
[35] A. Cerezo, G.D.W. Smith, P.H. Clifton, Appl. Phys. Lett. 88 (2006) 154103.
[36] B. Gault, A. Vella, F. Vurpillot, A. Menand, D. Blavette, B. Deconihout, Ultramicroscopy 107 (2007) 713–719.
[37] F. Vurpillot, B. Gault, A. Vella, M. Bouet, B. Deconihout, Appl. Phys. Lett. 88 (2006) 094105.
[38] D.Y. Li, Y. Wu, R. Fan, P.D. Yang, A. Majumdar, Appl. Phys. Lett. 83 (2003) 3186–3188.
[39] Dave Larson, Imago Scientific Instruments, Inc.; Private communication.